Sublimation and Oxidation Measurements of Graphite and Carbon Black at High Temperatures in a Shock Tube Using Absorption Imaging and Thermal Emission

Colton Willhardt^a, Damon Chen^a, Kyle Daniel^b, Daniel Guildenbecher^b, Nick Glumac*^a

- ^a Department of Mechanical Science and Engineering, University of Illinois at Urbana-Champaign, 1206 W Green St, Urbana, IL 61801
- b Sandia National Laboratories, Albuquerque, NM, 87123, USA
- * Corresponding author, glumac@illinois.edu

Abstract

Surface mass loss rates due to sublimation and oxidation at temperatures of 3000-7000K have been measured in a shock tube for graphite and carbon black (CB) particles. Diagnostics are presented for measuring surface mass loss rates by diffuse backlit illumination extinction imaging and thermal emission. The surface mass loss rate is found by regression fitting extinction and emission signals with an independent spherical primary particle assumption. Measured graphite sublimation and oxidation rates are reported to be an order of magnitude greater than CB sublimation and oxidation rates. It is speculated that the difference between CB and graphite surface mass loss rates is largely due to the primary particle assumption of the presented technique which misrepresents the effective surface area of an aggregate particle where primary particles overlap and shield inner particles. Measured sublimation rates are compared to sublimation models in the literature, and it is seen graphite shows fair agreement with the models while CB underestimates, likely a result of the particle shielding affect not being considered in the sublimation model.

Keywords

Shock tube, High temperature, Sublimation, Oxidation, Soot, Carbon

Novelty and Significance Statement

The novelty of this study is that surface mass loss rates of solid carbon are measured in high temperatures that are to be expected in a high explosive fireball. The way in which the optical diagnostics are modified and applied, and the measured signals are processed, is also novel. The significance of the work is that the measurements aid soot modeling in combustion environments at high temperatures by providing surface mass loss rates in novel conditions, eliminating the need to extrapolate measurements from lower temperatures, and showing the potential impact of particle morphology on predicted mass loss rates from sublimation and oxidation.

CRediT Authorship Contribution Statement

C.W. Conceptualization, Performed research, Wrote the paper. **D.C.** Conceptualization, Performed research. **K.D.** Conceptualization, Performed research, Reviewed and edited the paper. **D. G.** Conceptualization, Reviewed and edited the paper. **N.G.** Conceptualization, Supervision, Funding acquisition

1 Introduction

Soot is the dominant contributor to optical emission in high explosive (HE) fireballs, thus understanding the reactive and optical properties of soot within a detonation fireball is critical to improving the fidelity of optical signature predictions of these events. Mass loss rates of carbon particles are also important to

modeling laser induced incandescence. LII modeling is based on a particle energy balance, where the energy loss due to sublimation is critical to determining the particle energy [1–3]. Additionally, solid carbon is often considered as a material for use in high temperature environments, such as nuclear reactors, where solid carbon ablative properties must be known for estimates of component lifetime.

The need to measure solid carbon mass loss rates at temperatures of 3000-7000 K is motivated by fireball temperature measurements reported in the literature. Continuum emission generally indicates temperatures of the condensed phases around 3000-4000 K, however early time measurements of atomic and molecular emission indicate layers of hot gas as high as 15000 K [4]. It is likely that solid carbon present in the mixing layer between the high temperature shock heated air and cooler post detonation products is heated to its sublimation temperature [5], and quickly ablates into gaseous products. This mixing of solid carbon, such as soot and diamond, into hot gas necessitates the characterization of optical and ablative properties at the temperatures.

Solid carbon is subject to mass loss by surface oxidation. Several studies have measured and modeled rates of surface oxidation for solid carbon allotropes in a variety of environments [6–10]. Josephson compiles several experiments for modeling soot oxidation, all of which are experiments in flames where temperatures do not exceed 2000 K [11]. There are soot oxidation measurements in heterogeneous shock tubes reported in the literature [8,9], but to the best of the authors knowledge the highest gas temperature tested is 4000 K. Additionally, surface mass loss measurements of soot aggregates in a shock tube employ the independent spherical primary particle assumption when processing signal decay signals, likely overestimating the effective surface area of a fractal aggregate particle and thus underestimating the true surface mass loss rate.

The independent spherical primary particle assumption is common when modeling fractal aggregate particles. This simplification assumes that primary particles within the aggregate are non-interacting and non-overlapping with each other, simplifying particle modeling [3,8,9]. This simplification, as indicated in the results section, can introduce significant error when primary particles in an aggregate overlap, reducing the effective surface area.

The sublimation temperature of solid carbon at 1 atm, assuming C_3 is the sublimation product, is 4137K [1,12,13], so sublimation will significantly contribute to particle mass loss and energy in high gas temperature environments. The surface mass loss rate due to sublimation is given by

$$\omega_{sub} = \frac{W_v \alpha_M p_v(T_s)}{R_p T} \left(\frac{R_m T_s}{2\pi W_v}\right)^k \tag{1}$$

where W_v is the atomic mass of subliming species, p_v is the vapor pressure of subliming species, R_m and R_p are the gas constant in effective mass and pressure units respectively, T_s is surface temperature, k is a constant derived from kinetic theory, and α_M is the mass accommodation coefficient for subliming species, often referred to as an evaporation coefficient [3]. It is known that multiple carbon species, C_{1-n} , sublimate from solid carbon [12,14]. There are several sources for the vapor pressures of carbon species given in the literature and values used for the mass accommodation coefficient vary based on the sublimed carbon species considered [12,13,15]. Michelsen [3] reviews and compares laser induced incandescence models of soot, where the main difference in the sublimation rate between each model are choices of p_v , α_M , and subliming species in equation 1.

The mass accommodation coefficients found in the literature and used for modeling soot sublimation are based on solid graphite measurements, where α_M is assumed to be constant. It is expected that the

accommodation coefficient will be morphology, temperature, and pressure dependent and should be less than unity [13]. It has been noted that there is little fundamental basis for the values of mass accommodation coefficients used in the literature [16], and there are no measurements found in the literature for sublimation rates of carbon particulate in a shock heated environment. Measurements of surface mass loss rates for carbon allotropes at high gas temperatures are necessary to fill this gap.

In this paper we describe novel diagnostic techniques for measuring surface mass loss rates of condensed phase particulates in both the geometric and Rayliegh regime under an independent spherical primary particle assumption. Graphite is used as a test sample as much of the modeling of carbonaceous particles is based on graphite thermodynamic data and it has simple particle shape, and CB is chosen as it closely resembles soot morphology and is easy to acquire commercially. We then present graphite and CB sublimation rates with fits to the mass accommodation coefficient. Measured oxidation rates for graphite and CB are fit with Arrhenius parameters.

2 Experimental Setup

2.1 Heterogeneous Shock Tube

The heterogeneous shock tube at the University of Illinois enables injection of a stationary particle cloud in front of optical access ports in a well described high temperature and pressure bath gas. The bath gas temperature and pressure are computed using the well-established normal shock relations [17] with measured initial gas conditions (incident shock speed, fill gas temperature, fill gas pressure, and fill gas composition) and assumed equilibrium gas conditions with NASA Chemical Equilibrium Application [18]. The shock tube is divided into two sections with a diaphragm. The driven section (test section) is 8 m long and 8.9 cm

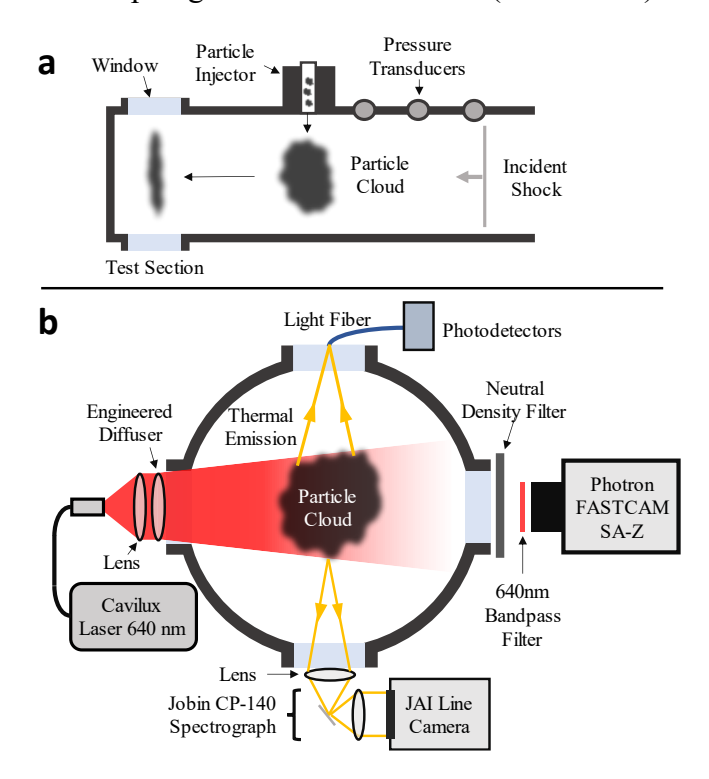


Figure 1 – (a) Schematic showing particle injection into the shock tube (top view) (b) cross section of test section with particle surface mass loss diagnostics (side view from the endwalls perspective)

internal diameter. The gas composition in the driven section is controlled by vacuuming the chamber to 10^{-2} torr and filling with the test gas to the required initial pressure to get the desired conditions behind the reflected shock.

Particulate is introduced into the test section using a pneumatic injector. Less than 1 mg of particulate is loaded into a small reservoir mounted on the exterior of the tube wall 0.5 m upstream from the optical access. The reservoir is vacuumed and has a mesh screen and 50 µm hole through the wall of the shock tube for injecting the particles through. Using a pressurized stream of the test gas the particulate is injected into the test section as a dilute cloud. The driver pressure at which the diaphragm bursts is known, so the particle injector is activated immediately before the burst pressure is reached and the incident shock wave is propagated into the test section. A diagram of the shock tube configuration is shown in Figure 1a. Across the incident shock the temperature and pressure increase at nearly a step function. The incident shock flow contacts the particles, pushing them into the optical path of the test section. The incident wave reflects off the end wall and contacts the particle cloud again as shown in Figure 3b, compressing the particle cloud to a thin sheet, decreasing the particle cloud velocity to zero through drag forces, and increasing the temperature and pressure of the gas again. The individual particle temperature rises at a near step function, but the shock wave takes several microseconds to move through the entire particle cloud as shown in the sequency of Figure 3a-c. It is assumed that the cloud is diffuse enough that particles are non-interacting. The test time is ended by the arrival of a reflected shock off the contact surface. The test time is approximately 500 µs for all tests in this work, long enough for the particles to ablate into the gas phase partially or completely.

Argon-oxygen gas mixtures are used for the fill gas. Two conditions are tested; 100% Ar to isolate sublimation, and 95% Ar 5% O_2 to introduce oxidation. All reflected shock conditions are at 3 ± 0.3 Bar.

Measurement uncertainties are propagated using accepted linear error propagation methods [19–21]. Signal uncertainties are input into least square and orthogonal distance regression fitting schemes, and propagated uncertainties in fit parameters are found using the diagonals of the covariance matrix [20,21]. Uncertainties reported correspond to 95% confidence intervals.

2.2 Particle Sizing

A particle size distribution is necessary to fit the surface mass loss rate to extinction and emission signals. The Carbon Black (Alfa Aesar, 45527) and graphite (Alfa Aesar, 14736) used were collected after injection in the test section and sized by transmission and scanning electron microscopy, respectively. Sample images and size distributions are shown in Figure 2. The mean diameter of the CB primary particles is 37 nm, and 4.5 μ m for the graphite. The size distributions fit well against a log-normal distribution with $\mu = 3.607 \pm .017$ and $\sigma = .273 \pm .016$ for the CB sample, and $\mu = 8.357 \pm .015$ and $\sigma = .273 \pm .014$ for the graphite sample.

$$f(R) = \frac{1}{\sqrt{2\pi}R\sigma} exp\left(-\frac{(\ln(R) - \mu)^2}{2\sigma^2}\right)$$
 (2)

Where R is the initial particle radius and f(R) is the particle size distribution. For processing the results shown in this paper, the log-normal fit described by equation 2 was used.

2.3 Mass Loss from DBI Extinction Imaging

One of the primary diagnostics used to measure surface mass loss rates from oxidation and sublimation was diffuse backlit illumination (DBI) extinction imaging. Park and Appleton [8] present a laser absorption technique for measuring oxidation rates of soot in a shock tube, and we modify this technique to particle cloud absorption imaging of a diffusely backlit field. The diffuse backlit technique minimizes beam steering

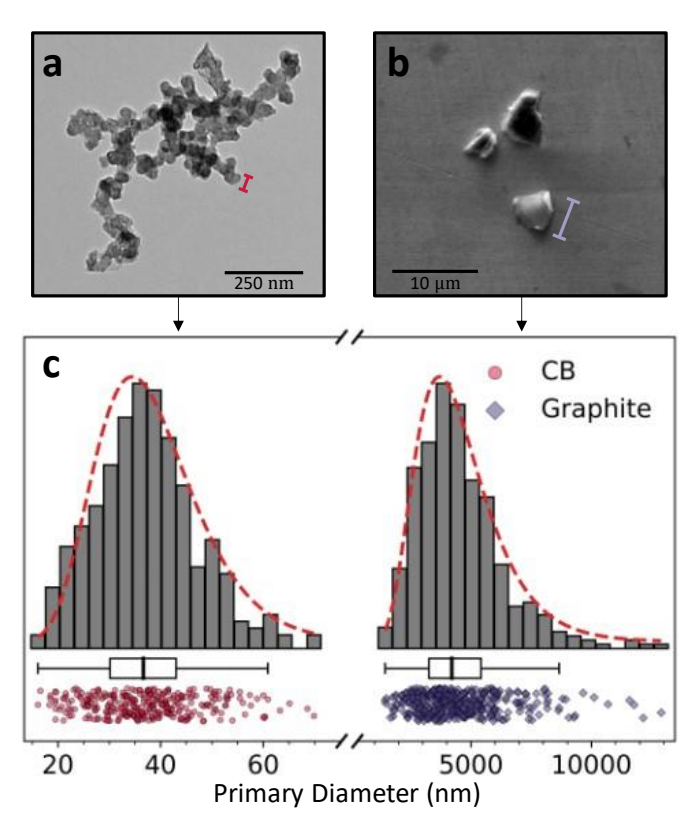


Figure 2 – (a) TEM image of CB (b) SEM image of graphite (c) Carbon Black and graphite size distributions with log-normal fits

effects. Westlye et al [22] give a detailed review of the technique. Imaging also enables averaging over the entire particle sheet, while offsetting for the time that the particles contact reflected shock heated gas, decreasing uncertainty correlated to particle movement during the test time.

A Photron Fastcam SA-Z, as shown in Figure 1b, is used and is operated at 400 kHz with a resolution of 256x100 px and exposure time of 160 ns. The pulse from the laser is synced with the exposure on the Photron and pulsed for 70 ns. Light from the laser is collimated using a 3" lens and passed through an engineered diffuser into the test section through 1" thick sapphire windows. It is necessary that the laser is significantly stronger than thermal emission from the particle cloud so as not to image particle emission. Therefore, a neutral density filter and bandpass filter at 640 nm was used to decrease the particle light emission intensity.

With imaging, the particle cloud does not need to be perfectly in line with a focused laser beam, and instead just needs to be within the width of the imaged field and diffuse backlight. This is important as it is desired to inject a minimum amount of particulate into the test section so as not to interfere with the bath gas temperature calculations, and for the particle cloud to compact to a thin sheet (~1mm) after impacting the reflected shock. Getting a thin cloud of particulate exactly into a laser path is challenging and results in a low experimental success rate with more uncertainties in the data. With extinction imaging the particle cloud can land anywhere within the imaged field, making the experiment easier to complete and process.

Typical DBI extinction imaging of a particle cloud during a test event is shown in Figure 3. The cloud is seen being carried into the test section with the incident shock flow (Figure 3a), contacting the reflected

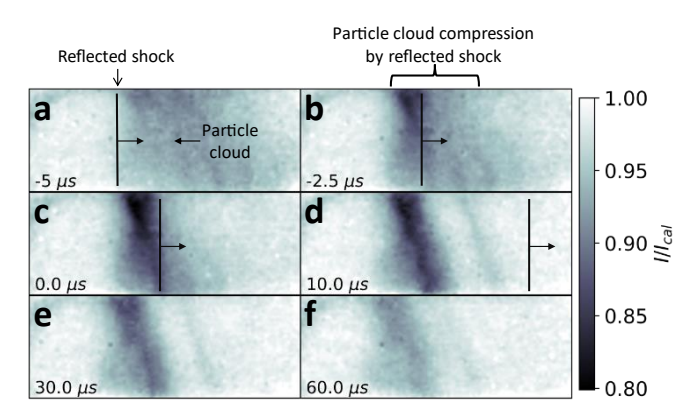


Figure 3 – DBI extinction imaging from 5000K 100% Ar Carbon Black shot. Perspective is with the shock tube end wall on the left and particle injection location on the right. Color is related to the optical density as shown by the color bar.

shock in the middle of the test section (Figure 3b-c), and ablating in reflected shock gas conditions (Figure 3d-f).

Park [8] derives the laser absorbance signal of particles subject to a surface mass loss rate, ω ($g \cdot cm^{-2} \cdot s^{-1}$), and their technique is modified and applied to the extinction images measured here. For a fixed wavelength and complex index of refraction for a spherical particle in the Rayleigh regime (x < 1 where $x = 2\pi r/\lambda$), the extinction due to absorption is directly proportional to volume fraction [23,24]. The initial particle radius, R, is given by the size distribution f(R). Integrating across the size distribution, a decrease in signal at the time of maximum absorption, t = 0, is proportional to

$$I_f - I_0 \propto \alpha \frac{4}{3} \pi \int_{R=0}^{\infty} f(R) R^3 dR \tag{3}$$

Where I_f is defined as the light intensity per pixel without particle attenuation, I_o is the signal level at peak attenuation per pixel, and α is the absorption constant. The notation, while non-standard, is kept the same as used by Park. The drop in signal per pixel at any time t is then written as

$$I_f - I(t) \propto \alpha \frac{4}{3} \pi \int_{R=0}^{\infty} f(R) r^3 dR \tag{4}$$

Where r = r(t, R) and is the radius of a soot particle with initial radius R at some time t. I is the intensity of the absorption signal at any time $t \ge 0$. The division of equations 4 and 3 will cancel out the extinction constants assuming they are constant with particle size and result in the equality defined as y_{abs} .

$$y_{\text{abs}} = \frac{I_f - I}{I_f - I_0} = \frac{\int_{R=0}^{\infty} f(R) r^3 dR}{\int_{R=0}^{\infty} f(R) R^3 dR}$$
 (5)

f(R) and R are known and y_{abs} is measured directly. The radius of the particle, r, is related to the mass of the particle which is subject to change by the surface mass loss rate, ω . The particle radius at any time t assuming spherical particles is then

$$r = \begin{cases} R - \frac{\omega}{\rho}t & R > \frac{\omega t}{\rho} \\ 0 & R \le \frac{\omega t}{\rho} \end{cases}$$
 (6)

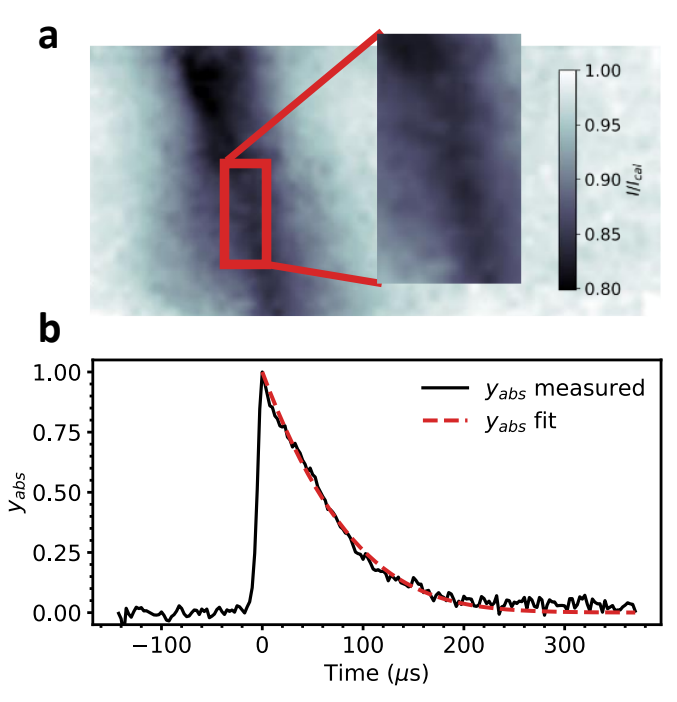


Figure 4 – (a) crop of pixels chosen for processing; (b) y_{abs} for the region of pixels in a with time offset to reflected shock contact and signal fit for ω ; 5000K 100% Ar Carbon Black

All terms in equation 5 are now known except ω , with the density being calculated with the temperature dependent polynomial [2]. Because the model is formulated with initial radius R and size distribution f(R) at t=0, it does not consider the possible change in the size distribution as time progresses. However, under the assumption that mass loss is purely a surface process and particle overlap does not affect the mass loss for individual particles, the change in radius for all particles is constant over time as shown by equation 6. Therefore, under these assumptions, the size distribution is constant over time for any particle with initial radius R. It is assumed that surface and gas temperature remain constant and that ω is constant through the test time. The constant surface temperature assumption holds well based on temperature measurements shown later, however it is not known how ω changes with radius and is assumed to be constant. Park derives an analytical solution to equation 5 given their tested particle size distribution and solves for the root at y=0.5 resulting in the formula Park uses for mass loss from a characteristic time, τ .

$$\omega = .33 \frac{R_m \rho}{\tau} \tag{7}$$

Park uses equation 7 as a simple expression to calculate mass loss by measuring the characteristic time τ on the oscillogram. This simplified method introduces additional uncertainty as only two points on the measured signal are used. Instead, the entire measured signal y_{abs} can be fit numerically using a least square fitting technique where ω is the model input.

The derivation is dependent on the optically thin assumption, where light attenuation is linear. Most signals processed in this paper have a peak absorbance, I/I_{cal} , greater than .9. Even at this absorbance there is error from the optically thin assumption. However, not making the optically thin assumption means the absorption coefficients in equation 5 no longer cancel and must be known. The absorption coefficient is not well characterized as a function of particle morphology and temperature, so the optically thin assumption is assumed to introduce less error.

The process for deriving y_{abs} for a particle in the Rayleigh regime can be applied to the geometric regime, where absorption is proportional to surface area [24] and the radius term in y_{abs} is now squared. The geometric regime derivation is used for processing the graphite signals. The size parameter, x, for the graphite and CB primary particles are 22.1 and 0.182, respectively. The Rayleigh approximation is likely more valid for CB, as x will decrease over the test time, and less valid for graphite. However, it is chosen to make these approximations to make interpretation of already complex measurements as simple and reproducible as possible.

The time at which the reflected shock contacts the particles must be offset for each pixel across the horizontal axis as the shock travels with finite speed through the particle cloud. No spatial filtering of the image is performed as this would smear the location of the shock between pixels. Filtering of the averaged signal y_{abs} is also not necessary, as the averaging of many pixels results in good signal to noise ratio. The emission intensity from the Cavilux laser drops off over time which must be corrected for, so a calibration video is taken immediately before the test and noted as I_{cal} .

2.4 Mass Loss from Emission

Particle thermal emission is measured and used as an additional method to calculate the surface mass loss rate. Emission is measured with 3 amplified photodetectors (2 PDA10A2, 1 PDA10CS2). Light is collected from a single fiber, spectrally split via dichroic mirrors, and filtered at 700, 905, and 1310 nm with 10 nm FWHM bandpass filters into each photodetector respectively. The disadvantage to the emission diagnostic is that emission is integrated over a collection area much larger than the pixel area from the absorption imaging technique, making interpretation of the signal decay harder as the reflected shock takes finite time to propagate through the collection area.

Equation 5 is derived assuming zero spatial dimensions – all particles in a pixel area are instantaneously heated by shock heated gas at the same time. The 0-D simplification is fine for the absorption measurement as t=0 can be offset for all pixels, and the pixel area is relatively small. However, the 0-D simplification poses a challenge for the emission measurement performed here as light is collected over an area. This additional dimensionality can be modeled, but challenges arise in fitting a model with a spatial dimension as there are several additional input parameters. In this work a 0-D model is derived and used for fitting ω to emission signals. A 1-D model is also derived and discussed in the appendix but is only used to verify the shape of the measured signal and as a tool to quantify the error associated with the 0-D model.

The emissivity of a soot particle has wavelength and particle size dependance [3].

$$\varepsilon \propto \frac{r^n}{\lambda \gamma} \tag{8}$$

Integrating Planks law [3], the thermal radiation of a soot particle is

$$Q_{rad} = \frac{199\pi^3 D^{2+n} (k_B T)^{4+\gamma} E(m)}{h(hc)^{2+\gamma}}$$
(9)

Signal intensity measured by the photodiode, I, is directly proportional to Q_{rad} . Therefore, for any particle size distribution, f(R), the measured signal intensity I at any time t is

$$I(t) \propto \int_0^\infty f(R)Q_{rad}(r)dR \tag{10}$$

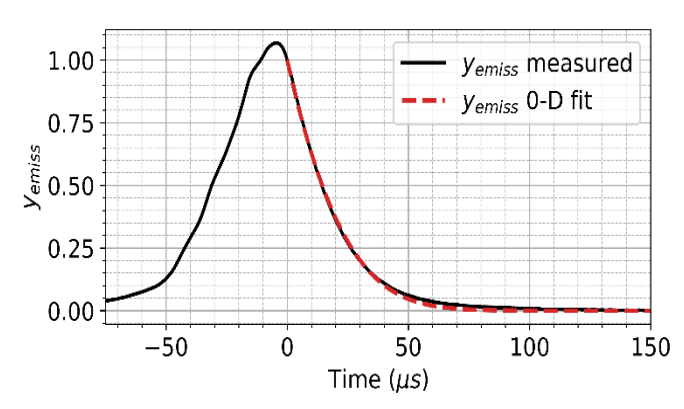


Figure 5 – Measured emission signals with 0-D emission fit. 5000K 5% O_2 CB Where R is the initial particle radius, and r(t, R) is the radius at any t > 0 for a particle with initial radius R. I_0 is defined as signal intensity at t = 0.

$$I_0 \propto \int_0^\infty f(R)Q_{rad}(R)dR \tag{11}$$

Dividing equations 10 and 11 to cancel out like terms and substituting equations 9 and 6, the 0-D model is derived and given by equation 12.

$$y_{emiss} = \frac{I}{I_0} = \frac{\int_0^\infty f(R) \left(R - \frac{\omega t}{\rho} \right)^{2+n} dR}{\int_0^\infty f(R) R^{2+n} dR}$$
(12)

We use the approximation of 1 for n in the Rayleigh regime and 0 in the geometric regime [23,24].

An emission signal fit with equation 12 is shown in Figure 5. Notice that t=0 is not defined as the time of peak intensity. Setting t=0 to the peak of the emission signal in Figure 5 results in a poor 0-D fit for equation 12 as the signal does not have a sharp rise and fall because of the spatial dimensionality of the measurement. t=0 is found by optimizing the squared residual between the times of peak signal intensity and maximum rate of signal change in the negative direction. Figure 6 shows residuals and best fit ω for equation 12 for varying t=0.

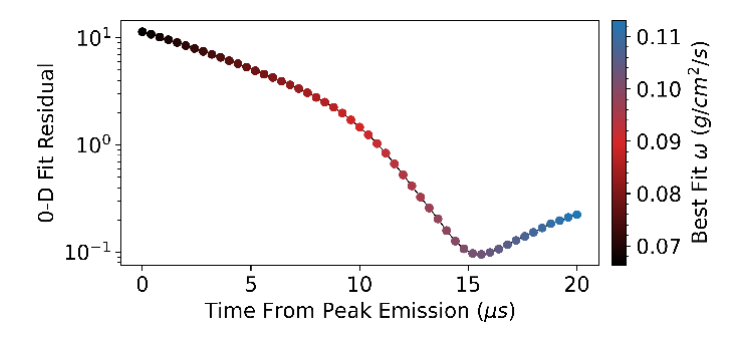


Figure 6 – Residuals of 0-D model fitting against emission signal for determining t_0

2.5 Temperature Fitting

A spectrometer is used to measure the condensed phase blackbody emission for fitting surface temperature and identifying gas products of particle mass loss. The system is a Jobin Yvon CP-140 spectrograph (f/2, 325-650 nm, 1 nm resolution), with a JAI SW-2000M-CL-80 monochrome line scan

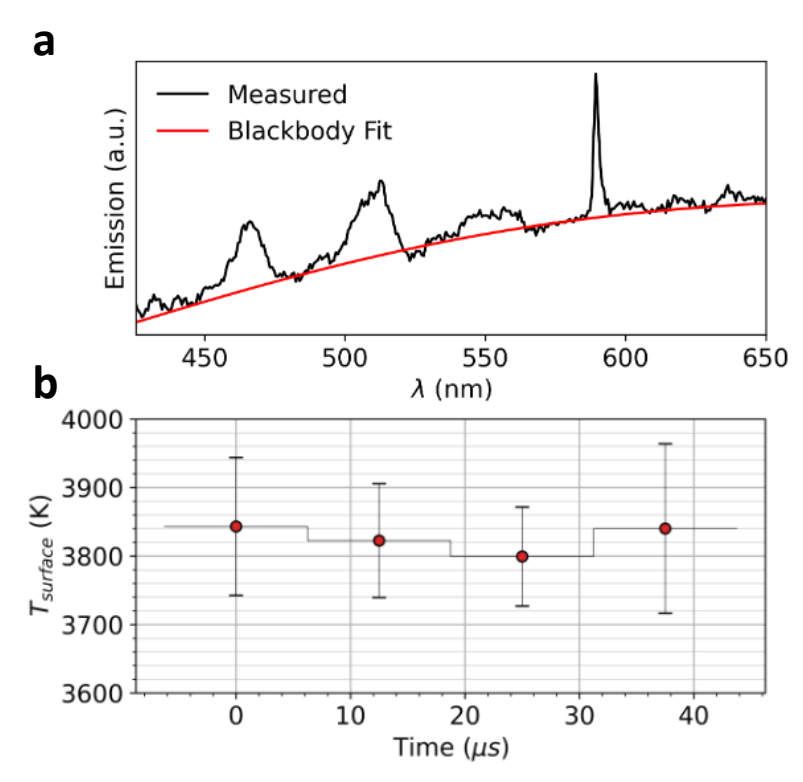


Figure 7 – (a) Spectrum from 12.5 μs exposure and blackbody fit (b) Temperature fits for one shot, vertical bar corresponding to 95% confidence interval and horizontal bars corresponding to exposure time

camera imaging at 80 kHz. Standard wavelength and intensity calibration is performed with hollow cathode and tungsten lamps. Light is collected and focused with a lens system from a side window of the test section, with an iris limiting the collection area to a point on the particle sheet.

The background emission signal is fit with a combination of a median filter and polynomial baseline fitter [25]. Temperature is found for both CB and graphite from fitting Planck radiation with a wavelength dependent emissivity to the background emission signal. The Rayleigh approximation gives $\gamma = 1$ for the emissivity wavelength dependance $\varepsilon \propto 1/\lambda^{\gamma}$ [23,24]. But a deviation from 1 is sometimes observed [3], so the wavelength dependance γ is also fit. A fit to a single 12.5 μs exposure is shown in Figure 7a. Fit values of γ for CB fall between .2 and .5, varying with temperature and test time. It is observed in Figure 7b that surface temperature is relatively constant through the test time, satisfying the constant temperature assumption made for the surface mass loss measurements.

3 Results and Discussion

The calculation of the surface mass loss rate, ω , from the decay signals is dependent on the applied model and assumptions. Decay signals are processed under the spherical primary particle assumptions according to the previous sections, leaving the surface mass loss rate data presented in as raw of a format as possible for ease of interpretation and suggestion of corrective factors that should be applied to the model.

Shown in Figure 8a are measurements of gaseous C_2 and CN during particle ablation. The presence of C_2 is not surprising as it is a known sublimation product of solid carbon [12], but the presence of CN is a bit more challenging to explain. Nitrogen has been measured in the chemical composition of soot [26]. Nitrogen could also be adsorbed onto the particle surface, and some is left in the test section after vacuuming ($<10^{-2}$

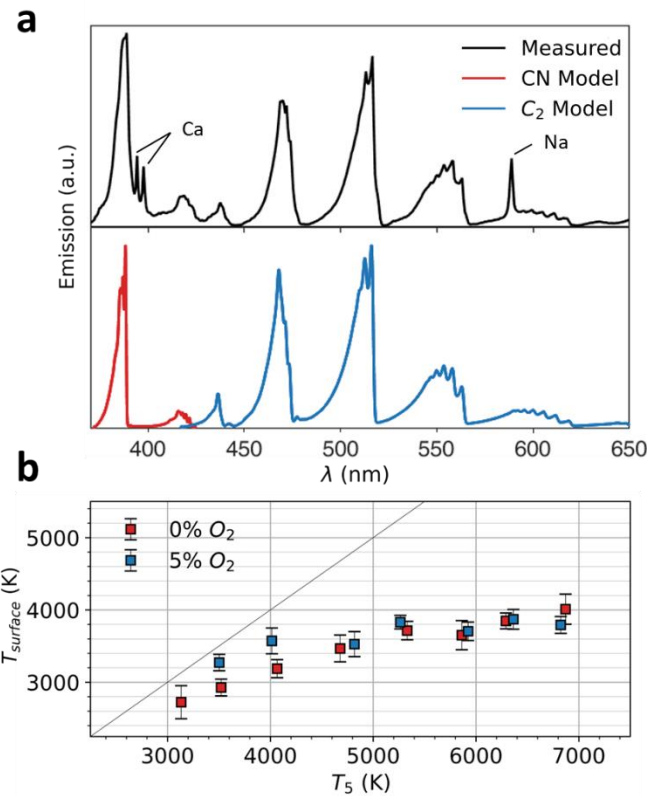


Figure 8 – (a) Identification of gaseous features in 6000K 100% Ar (b) Average CB surface temperature as a function of the gas temperature

torr). How the *CN* forms is currently unclear, whether it be a surface process or a reaction in the gas phase. Ca and Na are likely contaminants as their presence is consistently measured in our shock tube regardless of the tested particulate.

When the particle temperature approaches the sublimation temperature, the particle temperature deviates from the gas temperature, as shown in Figure 8b. It is expected that particle temperature is higher for the oxidizing case, as oxidation is exothermic [2,3]. The measured surface temperature is important for interpretation of sublimation rates, which are modeled as a function of the surface temperature [3].

The measured surface temperature of CB leveling off at 4000 K is in general agreement with temperature measurements in LII [5] where measured surface temperature as a function of incident light intensity levels off between 4000 and 4500 K. Although the particle heating mechanism varies between LII and the shock tube. In the shock tube, the particle is heated mostly by collisions with the bath gas. This creates an additional dynamic as gas sublimating from the particle surface will create pressure and concentration gradients that impede collisions between the bath gas and the particle surface.

Measured mass loss rates from absorption and emission diagnostic techniques for oxidizing and non-oxidizing conditions are shown in Figure 9. Carbon Black oxidation rate measurements from Cadman and Park [8,9] and the same partial pressure of oxygen have been digitized and show that our measurements of CB continue previously measured trends. It is observed that absorption measures the mass loss rate to be roughly 1.5 times greater than the emission measurement. This discrepancy is partially a result of assumptions in optical parameters when processing decay signals, i.e., particle cloud optical thickness affects, and absorbance and emission scaling based on the Rayleigh and geometric spherical particle

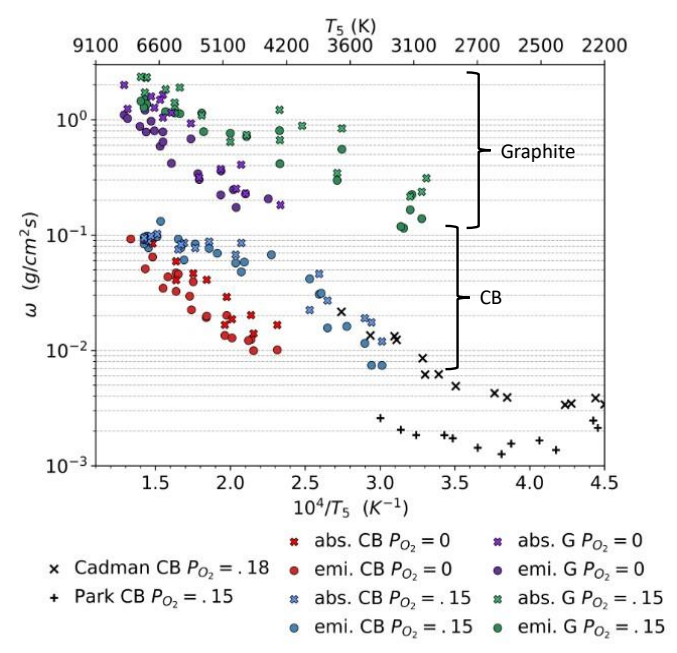


Figure 9 – Measured surface mass loss rates from emission and absorption compared to oxidation rates from the literature, where Cadman and Park are both in oxidizing conditions at similar partial pressures of O_2 .

approximations. The discrepancy is also impacted by the 0-D simplification when processing emission decay signals, and we would expect the absorption measurement to hold more accuracy. Most notably observed is the discrepancy between graphite and CB, which differ by nearly an order of magnitude.

3.1 Sublimation

Interpretation of measured sublimation rates are aided by comparison to sublimation models used in the literature. Figure 10 shows surface mass loss rates measured in 0% O_2 gas conditions, so the only contributor to mass loss is sublimation, and direct comparison to equation 1 can be made. The temperature is taken to be the measured particle temperature, as when $T_{surface}$ approaches the sublimation temperature it deviates from the gas temperature. Three models for the sublimation rate from the LII soot modeling literature are chosen for comparison and fitting to our measured rates, given in $Table\ I$. Detailed descriptions of the models can be found elsewhere [3]. It is important to note that extrapolation of current sublimation models overpredict our measurements of CB at high temperatures. The Clausius-Clapeyron for the vapor pressure used by Michelsen and Melton fit the graphite temperature dependance well but not the CB temperature dependance. Alternatively, the Charwath Antoine equation for vapor pressure fits the CB temperature dependance well and the graphite poorly.

The mass accommodation coefficient, α_M , is chosen as the single parameter for fitting the sublimation model given by equation 1 with model parameters in *Table 1*. The fit accommodation coefficients should be interpreted as bulk coefficients as a direct measurement of sublimed species concentrations is not made but rather assumed in the applied model. An Arrhenius equation with the gas temperature as the input has also been fit with parameters shown in Table 2. The Arrhenius fit to the gas temperature is only valid for the same gas conditions, as the rate of heat transfer by conduction between the particle and gas will vary with the gas composition, temperature, and pressure, altering the particle temperature and the sublimation rate.

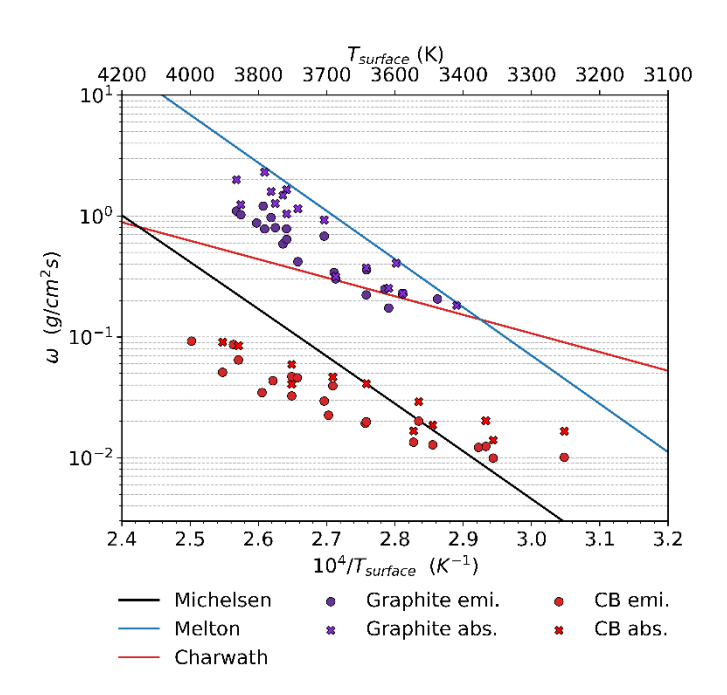


Figure 10 – Measured sublimation rates compared to sublimation models in the literature

The values cited in the literature [12,14], [5] for the mass accommodation coefficients for carbon species C_{1-n} are from graphite. These graphite-based estimates have then been directly applied to soot in LII modeling. It is likely that α_M has particle morphology dependance, resulting in different expected values for graphite and CB.

There are several possible factors for the discrepancy between graphite and CB sublimation rates. The most important factor is the effective surface area of the particles. It is assumed when processing the decay signals that the primary particles are spherical and don't overlap with other primary particles in the aggregate. There can be significant primary particle overlap in a fractal aggregate like CB as shown in Figure 2, so the effective surface area is less than what is predicted by the assumed model. The effect of overlap which is not currently accounted for would increase the calculated value of the surface mass loss rate for CB. Alternatively, the effective surface area of the graphite particles might be underestimated as the graphite

Table 1 – Parameters and α_M fit for sublimation models in the literature

There is a time term of the sum o						
Model	p_v	k	$lpha_M$	α_M CB fit	α_M G fit	
Michelsen[2]	b	0.5	$0.5; 0.5; 0.1; 10^{-4}; 10^{-4}$ for \mathcal{C}_{1-5}	-	a*: 10.1 ± 0.80 e*: 5.99 ± 0.36	
Melton[27]	c	0.5	1 for C_3	-	a: 0.631 ± .050 e: 0.374 ± .023	
Charwath[28]	d	0.4	0.9 for C_3	a: 0.143 ± .020 e: 0.100 ± .015	-	

a, e: absorption and emission fit, respectively

b:
$$p_{ref} \exp\left(-\frac{\Delta H_V}{R}\left(\frac{1}{T} - \frac{1}{T_{ref}}\right)\right)$$
, $p_{ref} = 1$ atm, $T_{ref} = 4603.48$, 4456.59, 4136.78, 4949.74, 4772.87 K for C_{1-5} c: $p_{ref} \exp\left(-\frac{\Delta H_V}{R}\left(\frac{1}{T} - \frac{1}{T_{ref}}\right)\right)$, $p_{ref} = 1$ atm, $T_{ref} = 3915$ K d: $p_{ref} \exp\left(-\frac{37500K}{T} + 9.579\right)$, $p_{ref} = 1$ atm

^{*:} Scaling factor against original set of α

Table $2 - \omega = A \cdot exp(-B/T)$ fit to absorbance and emission sublimation data

Data	$A\left(g^{1}cm^{-2}s^{-1}\right)$	B (K)
Absorption CB	1.49 ± 0.27	21000 ± 900
Emission CB	1.34 ± 0.07	22400 ± 300
Absorption G	55.5 ± 6.7	24000 ± 800
Emission G	32.7 ± 1.2	25200 ± 200

particles are independent and polyhedron like. The effect of a polyhedron particle where the surface area is more than what the spherical assumption makes would lower the calculated value of the surface mass loss rate. Overall, considering the effect of overlap and shape would decrease the gap between our CB and graphite measurements. The primary particle assumption is made in previous shock tube studies [8,9], with results digitized and plotted in Figure 9, showing Cadman CB measurements [9] agreeing with ours.

An overlap or shape factor could be considered in the sublimation model. To completely span the difference in sublimation rates between the particle types, a primary particle overlap of ~90% in the CB particles would be necessary. There are estimates of soot surface areas in the literature [29,30] and it is possible to make estimations of a particle overlap factor from images [31,32]. However, it is not known how this factor may change as the particle ablates, and this consideration is left for future studies.

The spherical primary particle assumption also influences optical properties. Specifically, the Rayleigh and geometric approximations for a sphere being applied to fractal aggregate CB particles and polyhedron like graphite particles. For CB, we would expect a deviation from n=3 and a deviation from n=2 for Graphite in $abs \propto r^n$. The optical properties can be more exactly calculated using accepted theory in the literature [33,34], but this is left for future studies.

There are other physical effects possibly contributing to the observed difference between graphite and CB, such as surface mass loss products creating larger pressures at the surface of the particle, lowering the mass accommodation coefficient. This effect would be dependent on particle size which is non-negligible given the dramatic difference in size between the graphite and CB particles tested.

3.2 Oxidation

In the oxidizing environment, there is surface mass loss due to both sublimation and oxidation. To isolate the oxidation rate, the mass loss contribution from sublimation must be subtracted from measured rates of mass loss in the oxidizing gas environment, such that $\omega_{ox} = \omega_{tot} - \omega_{sub}$. ω_{sub} is taken from the Arrhenius sublimation fits for the respective diagnostic shown prior. It is assumed that the sublimation rate is an independent process from oxidation. Some models of oxidation rates are taken from the literature for comparison [6,7,11]. It is not surprising that predicted rates span orders of magnitude between various models, as this observation has been made by others [9] with oxidation rates being sensitive to particle morphology, temperature, pressure, and oxidizer. Our measurements are expected to be valid only in the conditions which were tested. NASA CEA [18] calculates an equilibrium atomic oxygen concentration five times greater than diatomic at 4000 K, increasing exponentially with temperature, so it is assumed that atomic oxygen is the only oxidizing agent in the tested conditions. Although, it takes finite time for the vibrational degrees of freedom in O_2 to relax and cause dissociation. This time is generally short relative to the particle decay time but could have substantial effects at higher temperatures where the particle may decay faster than equilibrium is reached in the oxidizing species. This consideration is left for future studies. An Arrhenius equation is used to fit against the measurements.

$$\omega_{ox}(g \cdot cm^{-2} \cdot s^{-1}) = AT^n \exp\left(-\frac{E}{RT}\right) P_o \tag{13}$$

Where P_o is the partial pressure of atomic oxygen. Fit parameters are shown in Table 3 and plotted in Figure 11.

Data	$A\left(\frac{g}{cm^2\cdot s\cdot bar\cdot K^n}\right)$	n	$E_a\left(\frac{kJ}{mol}\right)$
Abs. CB	3.63e74	-18.2	758
Emi. CB	2.87 <i>e</i> 64	-15.7	695
Abs. G	2.87 <i>e</i> 32	-7.88	298
Emi. G	3.20e30	-7.22	336

Table 3 – $\omega = AT^n \exp(-E_a/RT) P_0$, fit to absorbance and emission oxidation data

It is observed that there is a strong temperature dependance, with the pre-exponential parameters taking large values. All measurements are made at a pressure of 3 Bar in 5% O_2 , so we are currently unable to determine the partial pressure dependance of oxygen, and it is assumed that the exponent is 1 on P_0 .

An order of magnitude discrepancy is still observed between graphite and CB particle species. Many of the same factors discussed in the sublimation section can be influencing the discrepancy observed in oxidation rates: morphology effects like overlap and shape on the effective surface area and optical properties, and diffusion of surface mass loss products impeding collisions with the bath gas and oxidizers.

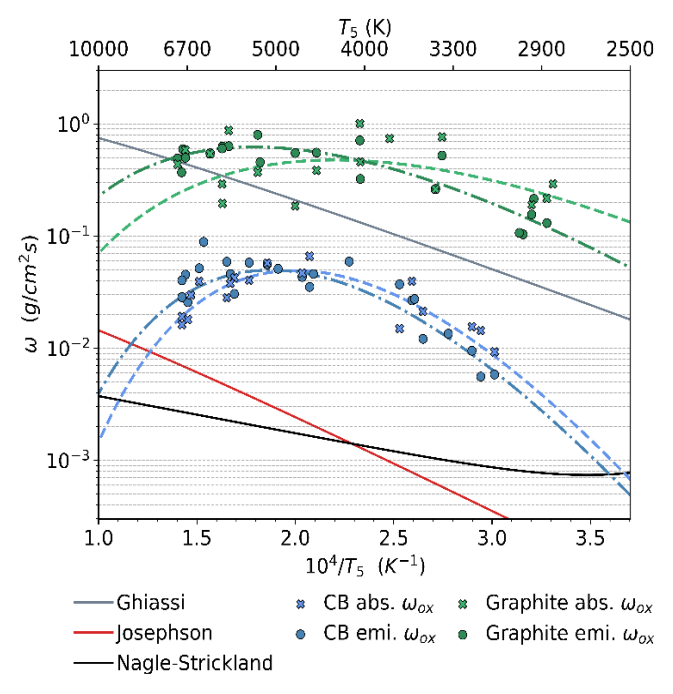


Figure 11– Measured oxidation rates, where oxidation is isolated by subtracting empirical sublimation fit, compared to some oxidation models in the literature. Dashed lines are Arrhenius fits to the measurements

4 Conclusions

Diagnostic techniques have been implemented for measuring surface mass loss rates of condensed phase materials in a shock tube. A simple spherical primary particle model has been applied for computing the surface mass loss rates from CB and graphite decay signals. Sublimation and oxidation models in the literature have been applied for comparison to measured surface mass loss rates.

Large discrepancies between graphite and CB are observed. A major factor in the discrepancy is likely particle morphology effects such as overlap in a fractal aggregate, or sharp polyhedron like features that deviate significantly from a spherical particle. More sophisticated models that consider particle morphology dependencies should be considered in future work. The shape dependencies likely change as the particle ablates, so measurements or coarse 3D modeling of particles are necessary to measure how the shape dependencies change during particle ablation.

The diagnostics presented here measure total particle mass loss and do not measure the individual product species of mass loss. Measurements of carbon cluster species at the surface of subliming particles are necessary for aiding in modeling the proportion of carbon clusters coming off the particle. It is also unclear if it is a good approximation to isolate oxidation rates from the total mass loss rate assuming sublimation is an independent process. Measurements of oxide species at the surface of the particle are necessary to elaborate on this issue.

Measurements of other carbon allotropes will aid in understanding the discrepancies observed between particle species: diamond, detonation soot, fullerenes, and altering particle sizes between the same species. Measurements in alternative bath gases would provide utility to particle modeling in more conditions. Conduction of heat between the bath gas and particle is dependent on bath gas composition, so different surface temperatures may be observed in gases with different conductivities. Oxidation rates will vary with different oxidizing species. Of interest are gas species that are expected in HE fireballs like N_2 , CO, CO_2 , and H_2O .

Appendix

A.1 1-D Model

A 1-D model is derived to verify the shape of measured emission signals and error quantification. The motion of a soot particle comes from the drag force, described by equation 14 where ρ_F is the fluid density, r is the particle radius, m_P is the particle mass, C_D is the drag coefficient, and U_F and U_P are the fluid and particle velocities respectively.

$$-\frac{\pi}{2}r^{2}\rho_{F}C_{D}(U_{P}-U_{F})^{2} = m_{P}\frac{dU_{P}}{dt}$$
(14)

The particle radius is described by Equation 6 and thermal radiation is described by equation 9. The heat transfer is simply modeled as

$$T_{P} = \begin{cases} T_{F} & T_{F} < T_{sublimation} \\ T_{sublimation} & T_{F} > T_{sublimation} \end{cases}$$
 (15)

The particles are small enough that the rise time for temperature is negligible. The flow parameters are calculated with Gordon McBride shock tube calculator [18] given an incident shock velocity. The particles

have a size distribution, f(R), and are given an initial spatial distribution after injection described by a gaussian. The collection efficiency is assumed to be a gaussian centered at the location of the light fiber.

A simulation space is populated with particles and the physics described is applied to each particle individually. The inputs to the model are

- $\omega (g/cm^2/s)$
- Size distribution, f(R)
- Flow conditions
- Initial cloud width FWHM, C_S
- Collection efficiency FWHM, C_E
- Shock tube and diagnostic dimensions

The inputs ω and the initial cloud width are not known. The particle cloud shape after contacting the reflected shock is strongly dependent on the starting cloud distribution after injection and will significantly change the emission signal. Results from the 1-D simulation are shown in Figure 12 with comparisons to a measured emission signal from similar test conditions. The initial cloud width and surface mass loss rate was tuned to give a similar signal shape, with values of 0.08 $g \cdot cm^{-2} \cdot s^{-1}$ and 0.23 m for the surface mass loss rate and full width half max of the initial particle distribution, respectively.

Fitting the 1-D model to measured signals is challenging due to too many initial parameters and is not used as a technique for extracting ω from the emission signals. However, the 1-D model is useful for validating the shape of measured signals and as a tool for error analysis in using the 0-D model.

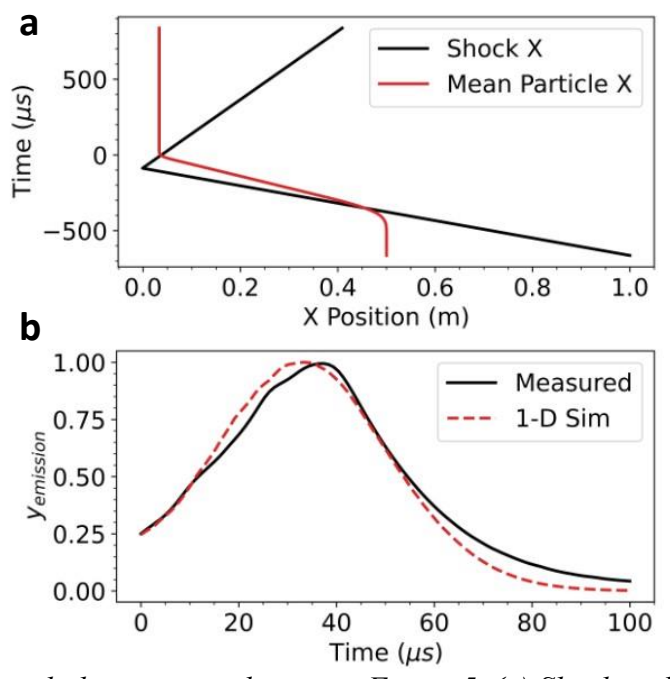


Figure 12 – 1-D simulation with the same conditions as Figure 5. (a) Shock and average particle location; (b) Simulated and measured (from Figure 5) emission

Acknowledgements

Sandia National Laboratories is a multimission laboratory managed and operated by National Technology & Engineering Solutions of Sandia, LLC, a wholly owned subsidiary of Honeywell International Inc., for the U.S. Department of Energy's National Nuclear Security Administration under contract DE-

NA0003525. This paper describes objective technical results and analysis. Any subjective views or opinions that might be expressed in the paper do not necessarily represent the views of the U.S. Department of Energy or the United States Government. The authors are thankful for Dr. Hope Michelsen for helpful discussions on soot modeling, and Neil Thakker, Lisa Mirsaliyeva, Paul Raducha, and Jun Shin for contributions to laboratory operation.

References

- [1] H.A. Michelsen, Understanding and predicting the temporal response of laser-induced incandescence from carbonaceous particles, J Chem Phys 118 (2003) 7012–7045
- [2] H.A. Michelsen, M.A. Linne, B.F. Kock, M. Hofmann, B. Tribalet, C. Schulz, Modeling laser-induced incandescence of soot: Enthalpy changes during sublimation, conduction, and oxidation, Appl Phys B 93 (2008) 645–656.
- [3] H.A. Michelsen, F. Liu, B.F. Kock, H. Bladh, A. Boiarciuc, M. Charwath, T. Dreier, R. Hadef, M. Hofmann, J. Reimann, S. Will, P.E. Bengtsson, H. Bockhorn, F. Foucher, K.P. Geigle, C. Mounaïm-Rousselle, C. Schulz, R. Stirn, B. Tribalet, R. Suntz, Modeling laser-induced incandescence of soot: A summary and comparison of LII models, Appl Phys B 87 (2007) 503–521.
- [4] N. Glumac, Early time spectroscopic measurements during high-explosive detonation breakout into air, Shock Waves 23 (2013) 131–138.
- [5] F. Goulay, P.E. Schrader, X. Lopez-Yglesias, H.A. Michelsen, A data set for validation of models of laser-induced incandescence from soot: Temporal profiles of LII signal and particle temperature, Appl Phys B 112 (2013) 287–306.
- [6] H. Ghiassi, I.C. Jaramillo, J.A.S. Lighty, Kinetics of Soot Oxidation by Molecular Oxygen in a Premixed Flame, Energy and Fuels 30 (2016) 3463–3472.
- [7] J.R. Walls, R.F. Strickland-Constable, Oxidation of carbon between 1000–2400°C, Carbon N Y 1 (1964) 333–338.
- [8] C. Park, J.P. Appleton, Shock-tube measurements of soot oxidation rates, Combust. Flame 20 (1973) 369–379.
- [9] P. Cadman, R.J. Denning, Oxidation rates of soot particulates by oxygen in the temperature range 1500–3500 K determined using a shock tube, J. Chem. Soc., Faraday Trans. 92 (1996) 4159–4165.
- [10] J. Nagle, R.F. Strickland-Constable, Oxidation of Carbon Between 1000-2000°C, in: Proceedings of the Fifth Conference on Carbon, Elsevier, 1962: pp. 154–164.
- [11] A.J. Josephson, N.D. Gaffin, S.T. Smith, T.H. Fletcher, D.O. Lignell, Modeling Soot Oxidation and Gasification with Bayesian Statistics, Energy and Fuels 31 (2017) 11291–11303.
- [12] H.R. Leider, O.H. Krikorian, D.A. Young, Thermodynamic properties of carbon up to the critical point, Carbon N Y 11 (1973) 555–563.
- [13] R.J. Thorn, G.H. Winslow, Vaporization Coefficient of Graphite and Composition of the Equilibrium Vapor, J Chem Phys 26 (1957) 186–196.
- [14] C.H. Wu, U. Mszanowski, J.M.L. Martin, The impact of larger clusters formation C5, C6, C7, C8, C9, and C10 on the rates of carbon sublimation at elevated temperatures, Journal of Nuclear Materials 258–263 (1998) 782–786.
- [15] L. Brewer, J.S. Kane, The Importance of Complex Gaseous Molecules in High Temperature Systems, J Phys Chem 59 (1955) 105–109.

- [16] T. Lehre, B. Jungfleisch, R. Suntz, H. Bockhorn, Size distributions of nanoscaled particles and gas temperatures from time-resolved laser-induced-incandescence measurements, Appl Opt 42 (2003) 2021.
- [17] John D. Anderson, Modern Compressible Flow: with historical perspective, 3:, McGraw Hill Education, 2003.
- [18] S. Gordon, B.J. Mcbride, NASA Reference Computer Program for Calculation Complex Chemical Equilibrium Compositions and Applications, Nasa, Cleveland, Oh, USA, 1994.
- [19] R.J. Moffat, Describing the uncertainties in experimental results, Exp Therm Fluid Sci 1 (1988) 3–17.
- [20] K.H. Burrell, Error analysis for parameters determined in nonlinear least-squares fits, Am J Phys 58 (1990) 160–164.
- [21] P.T. Boggs, J.R. Donaldson, Orthogonal Distance Regression, National Institute of Standards and Technology, Gaithersburg, MD, 1989.
- [22] F.R. Westlye, K. Penney, A. Ivarsson, L.M. Pickett, J. Manin, S.A. Skeen, Diffuse back-illumination setup for high temporally resolved extinction imaging, Appl Opt 56 (2017) 5028.
- [23] H. Moosmüller, R.K. Chakrabarty, W.P. Arnott, Aerosol light absorption and its measurement: A review, J Quant Spectrosc Radiat Transf 110 (2009) 844–878.
- [24] C.F. Bohren, D.R. Huffman, Absorption and Scattering of Light by Small Particles, Wiley, 1998.
- [25] D. Erb, pybaselines: A Python library of algorithms for the baseline correction of experimental data., (2022). https://doi.org/10.5281/zenodo.5608581.
- [26] R.L. Vander Wal, V.M. Bryg, M.D. Hays, Fingerprinting soot (towards source identification): Physical structure and chemical composition, J Aerosol Sci 41 (2010) 108–117.
- [27] L.A. Melton, Soot diagnostics based on laser heating, Appl Opt 23 (1984) 2201.
- [28] M. Charwath, R. Suntz, H. Bockhorn, Influence of the temporal response of the detection system on time-resolved laser-induced incandescence signal evolutions, Applied Physics B 83 (2006) 435–442.
- [29] D. Coelho, S. Bekki, J. Thovert, P.M. Adler, Uptake on fractal particles: 1. Theoretical framework, Journal of Geophysical Research: Atmospheres 105 (2000) 3905–3916.
- [30] S. Bekki, C. David, K. Law, D.M. Smith, D. Coelho, J. Thovert, P.M. Adler, Uptake on fractal particles: 2. Applications, Journal of Geophysical Research: Atmospheres 105 (2000) 3917–3928.
- [31] A.M. Brasil, T.L. Farias, M.G. Carvalho, A Recipe for Image Characterization of Fractal-Like Aggregates, J Aerosol Sci 30 (1999) 1379–1389.
- [32] A.M. Brasil, T.L. Farias, M.G. Carvalho, U.O. Koylu, Numerical characterization of the morphology of aggregated particles, J Aerosol Sci 32 (2001) 489–508.
- [33] T.L. Farias, M.G. Carvalho, U.O. Ko"ylu", G.M. Faeth, Computational Evaluation of Approximate Rayleigh–Debye–Gans/Fractal-Aggregate Theory for the Absorption and Scattering Properties of Soot, J Heat Transfer 117 (1995) 152–159.
- [34] A.J. Saltzman, A.D. Brown, K. Wan, J.L. Manin, L.M. Pickett, M.C. Welliver, D.R. Guildenbecher, Extinction Imaging Diagnostics for In Situ Quantification of Soot within Explosively Generated Fireballs, Propellants Explos. Pyrotech. 48 (2023).